Available online at www.sciencedirect.com
ScienceDirect
Trans. Nonferrous Met. Soc. China 33(2023) 1814−1826
Transactions of Nonferrous Metals Society of China
www.tnmsc.cn

High-temperature oxidation behavior of $Cu_{64}Zr_{36}$ metallic glass powders

Mao ZHANG[1,2], Yun-fei MA[1], Ting HUANG[1], Pan GONG[1],
Ying WANG[3], Hong-jun CAI[1], Qiao-min LI[4], Xin-yun WANG[1], Lei DENG[1]

1. State Key Laboratory of Materials Processing and Die & Mould Technology, School of Materials Science and Engineering, Huazhong University of Science and Technology, Wuhan 430074, China;
2. State Key Laboratory of Metastable Materials Science and Technology, Yanshan University, Qinhuangdao 066004, China;
3. School of Mechanical Engineering, Wuhan Polytechnic University, Wuhan 430023, China;
4. School of Mechanical Engineering and Automation, Wuhan Textile University, Wuhan 430073, China

Received 8 February 2022; accepted 13 July 2022

Abstract: $Cu_{64}Zr_{36}$ metallic glass powders were prepared via gas atomization. The high-temperature oxidation behavior of $Cu_{64}Zr_{36}$ metallic glass powders under the influence of internal factors (powder particle size) and external factors (oxidation temperature and oxidation time) was experimentally investigated by using XRD, DSC, TGA, SEM and TEM. The oxidation kinetics, oxide phase, surface morphology and microstructure of metallic glass powders were analyzed. The results show that $Cu_{64}Zr_{36}$ metallic glass powders form multiple layers of surface oxides after oxidation and the major components of the surface oxides are t-ZrO_2, m-ZrO_2, Cu_2O and CuO. The oxidation kinetics follows a double-stage parabolic rate law. The oxidation process is dominated by the inward diffusion of O anions and the outward diffusion of Cu cations. Thermodynamic analysis shows that the Gibbs free energy change of the oxidation reaction increases with the decrease of particle size, leading to a more rapid and thorough oxidation of the powder with a smaller particle size.

Key words: metallic glass powder; high-temperature oxidation; thermodynamic analysis; ionic diffusion; parabolic rate law

1 Introduction

Due to their unique amorphous structures, metallic glasses (MGs) exhibit many excellent properties, including high strength, superior hardness, strong resistance to wear and corrosion, large elastic limit, and favorable biocompatibility [1−5]. Therefore, MGs have long been considered to have broad application prospects in the manufacturing of high-performance parts [6−8]. However, due to the strong brittleness of MGs, cracking is prone to take place during load bearing at room temperature [9−11]. Hence, conventional manufacturing techniques, such as casting, forging, and welding, cannot be used to produce MG parts with large dimensions and complex structures due to the limitation of glass forming ability (GFA) and room-temperature brittleness [12,13]. Some scholars have suggested manufacturing large-scale MG parts via powder metallurgy, i.e., the sintering or additive manufacturing based on MG powders to overcome these difficulties, which has already been proven to be a feasible solution [14−17].

In powder metallurgy processes, the surface quality of powders is a crucial factor determining the performances of final parts, since the interfacial bonding of powders is the key step to achieving the

Corresponding author: Lei DENG, Tel/Fax: +86-27-87559815, E-mail: denglei@hust.edu.cn
DOI: 10.1016/S1003-6326(23)66224-7

designated mechanical performances. Currently, MG powders are mainly produced via mechanical alloying and gas atomization [18−21]. However, due to the limitation of vacuum control, oxygen contamination is inevitable during the preparation, consolidation, storage, transport, and utilization of MG powders. Moreover, frequently used Cu-, Zr-, and Ni-based MGs all have strong oxygen affinities, and surface oxidation is prone to take place [22,23]. What is worse, with the reduction of powder particle size, the influence of the surface oxide layer on the global performance of the particle becomes more significant due to the dramatic increase of the volume fraction of the surface oxide layer. The surface oxidation of MG powders changes their intrinsic properties and affects the interface bonding of sintering and additive manufacturing, thereby reducing the strength of final parts [24,25]. Therefore, surface oxidation becomes an inevitable obstacle for the application of MG powders in powder metallurgy. An in-depth understanding of MG powders' surface oxidation behaviors and mechanisms becomes a premise for the further engineering application of MG powder metallurgy processes and products.

Available studies concerning the oxidation of MGs mainly focus on the oxidation behaviors of the bulk metallic glasses (BMGs) within the supercooled liquid region (SCLR), at which BMGs present superplasticity and become very suitable for the thermoplastic forming. For example, HUANG et al [26] compared the oxidation kinetics of $Zr_{55}Cu_{30}Al_{10}Ni_5$ BMG and its crystalline counterpart and reported that the oxidation process was controlled by ionic diffusion. The diffusion process was dominated by the inward diffusion of O and outward diffusion of Zr within the first 60 h. But it was dominated by the inward diffusion of O and outward diffusion of Cu in the following 60 h, while the outward diffusion of Zr was suppressed. LIU and CHAN [27] reported that t-ZrO_2 and m-ZrO_2 were formed during $Zr_{55}Cu_{30}Al_{10}Ni_5$ BMG high-temperature oxidation, with t-ZrO_2 mainly formed in the outer layer while m-ZrO_2 concentrated in the inner layer. ZHANG et al [28,29] reported that multilayered oxide scales were formed during the oxidation of $Zr_{55}Cu_{30}Al_{10}Ni_5$ BMG.

Compared to numerous reports concerning the oxidation behaviors of BMGs, attention paid to the oxidation of MG powders is still rare. YAN et al [30] reported that the gas-atomized Cu-based MG powders experienced fierce surface oxidation at temperatures higher than its crystallization temperature, while the oxidation rate was slow at its glassy state. However, there is still much work to be done to acquire sufficient knowledge of oxidation behaviors and uncover the underlying mechanisms. Therefore, in this work, the high-temperature oxidation behavior of $Cu_{64}Zr_{36}$ MG powders was studied, and the evolution of surface morphologies and internal microstructures was characterized. The underlying oxidation mechanism was discussed based on experimental results and thermodynamics analyses.

2 Experimental

2.1 Preparation of $Cu_{64}Zr_{36}$ MG powder

The $Cu_{64}Zr_{36}$ MG was selected due to its relatively broad SCLR. First, high-purity Zr and Cu raw materials (purity >99.99 wt.%) were mixed according to the composition ratio. After repetitive melting at high temperatures, alloy ingots with homogeneous compositions were obtained. The MG powders were prepared via the inert gas condensation method [15]. The atomization temperature was 1523 K, the pressure was 3.3 MPa, and the atomizing medium was high-purity Ar gas. The prepared powders were then screened into three grades: 0−50, 50−100, and 100−150 μm, which are referred to as Powder A, Powder B, and Powder C, respectively. The screened powders' particle size distribution was verified using a laser particle size analyzer (Mastersizer 3000, Malvern Panalytical). The densities of prepared powders were measured by using an automatic envelope density analyzer (AEDA, GeoPyc1365, Micromeritic).

2.2 Isothermal oxidation treatment

Isothermal oxidation treatment was conducted using a thermal gravimetric analyzer (TGA, TGA8000, PerkinElmer) in artificial dry air. Before putting into the analysis crucible of TGA, the powders were treated with ultrasonic vibration to avoid agglomeration. The pressure was kept as the normal pressure, and the temperature was set as 673, 773, 873, and 973 K, respectively. The temperature range covered the glassy state, supercooled liquid state, and crystallization state of the prepared $Cu_{64}Zr_{36}$ MG powders. The heating/cooling rates

were both set as 100 K/min. Accordingly, the insulation periods were set as 30, 60, 90, and 120 min. Mass gain during high-temperature oxidation was continuously recorded. The total surface area S of powder samples was calculated based on Eq. (1).

$$S = 4\pi\left(\frac{3m}{4\rho\pi}\right)^{2/3} \quad (1)$$

where m is the total mass of the powder sample, and ρ is the density of the sample.

2.3 Materials characterization

XRD (XRD−7000S, SHIMADZU) was used for phase analysis of the prepared powders and oxidized powders. Differential scanning calorimetry (DSC, Diamond DSC, PerkinElmer Instruments) was used to measure the thermodynamic parameters of the prepared powders. A field-emission scanning electron microscope (FE-SEM, JSM−7600F, JEOL) was used to analyze the surface morphologies of the prepared powders and oxidized powders. Cross-section specimens for transmission electron microscopy (TEM) observation were prepared via focused ion beam milling (FIB, Helico Nanolab 600, FEI). In order to improve the electrical conductivity of the material and protect the fine features of the oxide surface, a thin layer of Au was coated on the oxidized particle before FIB milling. TEM observations were conducted by using a field-emission transmission electron microscope (FE-TEM, Tecnai G2 F30, FEI) operating at 300 kV. The chemical compositions of local regions were detected by using an energy disperse spectrometer (EDS, Inca X-Max 50, Oxford Instruments) attached to the FE-TEM.

3 Results and discussion

3.1 Structure and thermal stability of $Cu_{64}Zr_{36}$ MG powders

The particle size distribution of three grades of gas-atomized MG powders is shown in Fig. 1. It is indicated that the particle size presents a typical beta distribution. The densities of gas-atomized powders were measured to be 4.08, 4.23, and 4.38 g/cm^3 for Powder A, Powder B, and Powder C, respectively.

As shown in Fig. 2, Powder A and Powder B are entirely amorphous, while some crystalline peaks can be found in the pattern of Powder C, indicating that a small portion of Powder C is crystallized. Based on the DSC curves displayed in Fig. 3, the glass transition temperature (T_g) and crystallization onset temperature (T_x) of the gas-

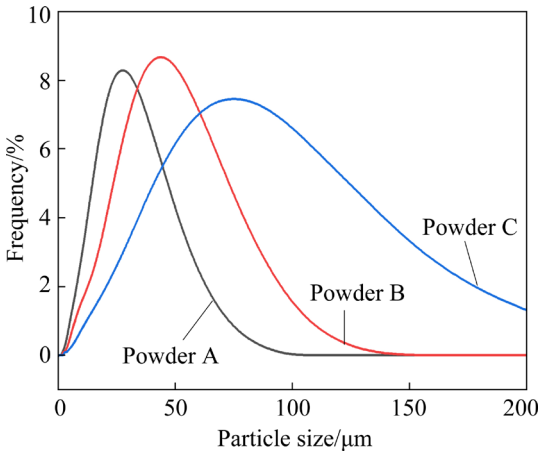

Fig. 1 Particle size distribution of gas-atomized $Cu_{64}Zr_{36}$ MG powders

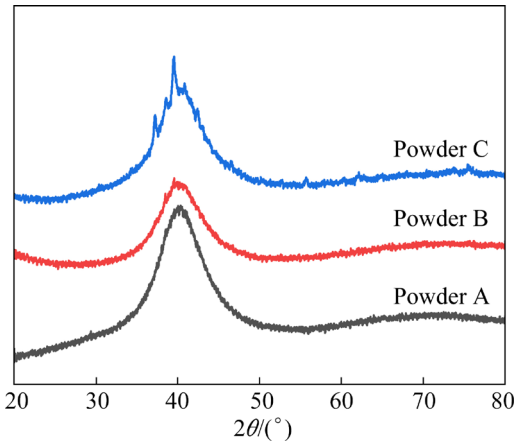

Fig. 2 XRD patterns of gas-atomized $Cu_{64}Zr_{36}$ MG powders

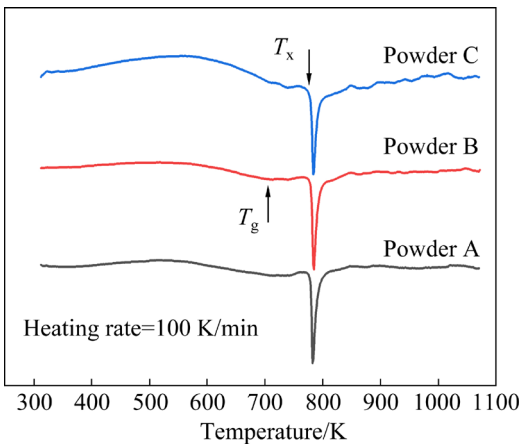

Fig. 3 DSC curves of gas-atomized $Cu_{64}Zr_{36}$ MG powders

atomized powders are determined to be 715 and 775 K, respectively.

Figure 4 shows the surface morphologies of gas-atomized $Cu_{64}Zr_{36}$ MG powders. Most particles are spherical or nearly spherical, and only a small amount of irregular particles exist. These irregular particles mainly include satellite particles and ellipsoid particles. Since the gas flow field in the gas atomization chamber is relatively complex, collision between particles will frequently take place. Smaller particles are more likely to be pushed to fly by airflow, and more quickly to get fully solidified. When fully solidified smaller particles collide with partially solidified larger particles, smaller particles will metallurgically adhere to larger particles, thus, forming satellite particles. The formation of ellipsoid particles is mainly caused by the insufficient spheroidization of larger droplets [31,32].

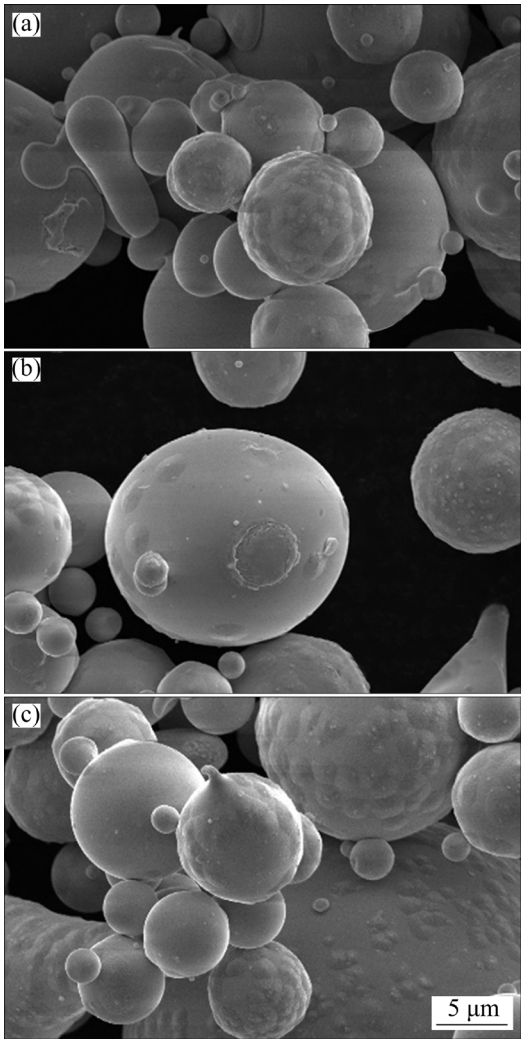

Fig. 4 Surface morphologies of gas-atomized $Cu_{64}Zr_{36}$ MG powders: (a) Powder A; (b) Powder B; (c) Powder C

3.2 Oxidation kinetics

Figures 5(a−c) show the oxidation kinetics curves of Powder A, Powder B and Powder C, respectively. It can be seen that at all temperatures, after a short period of time, the curves all begin to rise, which indicates that oxygen enters the sample and begins to react with elements with strong oxygen-affinities. The oxidation kinetics of $Cu_{64}Zr_{36}$ MG powders follows a double-stage parabolic rate law, consisting of an initial stage (the first stage) with fast oxidation and a subsequent stage (the second stage) with slow oxidation. It is thereby indicated that the oxidation is controlled by ionic diffusion, and the diffusion mechanism changes during prolonged oxidation [33]. The parabolic rate constants at both stages are calculated and plotted in Figs. 5(d−f). The parabolic rate constants of the first stage are generally high and change significantly with temperature rising, meanwhile, the parabolic rate constants of the second stage are low and basically unchanged. That is, the oxidation rates of $Cu_{64}Zr_{36}$ MG powders at different temperatures all decrease with the increase of time.

It can be seen from Figs. 5(d−f) that the particle size has a significant impact on the oxidation rate of MG powders. At 673 K, the first-stage oxidation rate of Powder A is several times greater than that of Powder B and Powder C, which further confirms that the reduction of particle size significantly accelerates the oxidation rate. The main reason is that compared with Powder B and Powder C, Powder A has the smallest average particle size, so it has a larger specific surface area, which leads to the increase of the volumetric fraction of weakly bonded surface atoms, which are more chemically active and more prone to oxidation. Therefore, at a lower temperature (673 K), Powder A will undergo extremely intense oxidation, thus forming a dense oxide film quickly. With the gradual thickening of the oxide film, the activity gradient across the oxide film will inevitably decrease, so that the oxidation rate will decline rapidly with the rise of temperature [34]. Therefore, the maximum parabolic rate constant of Powder A appears at 673 K. However, the specific surface area of Powder B and Powder C is small, and the oxidation rate is low at a lower temperature (673 K), which requires a higher temperature to drive the oxidation process. Therefore, the temperature

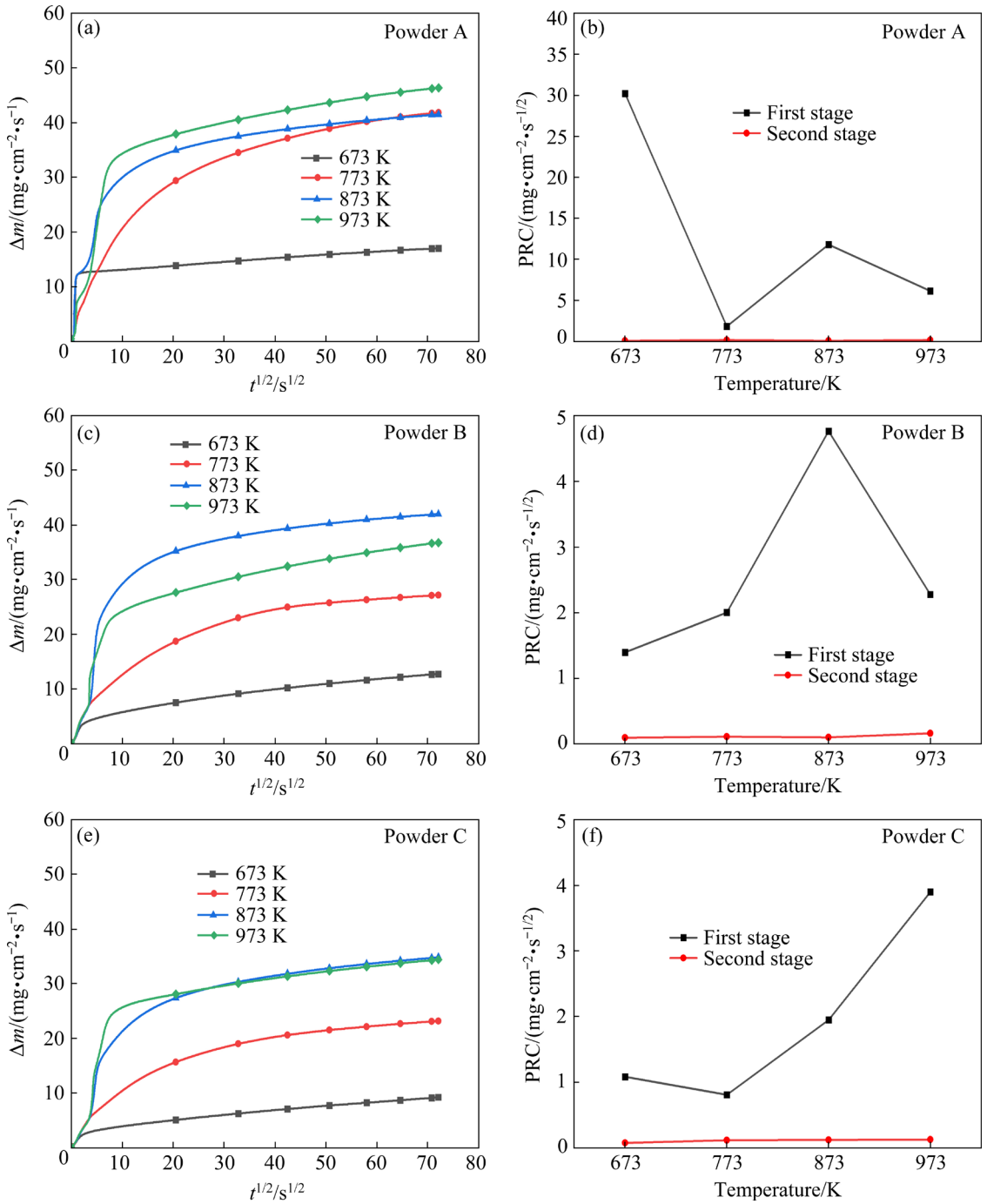

Fig. 5 Mass gain curves (a, c, e) and corresponding parabolic rate constants (PRC) (b, d, f) of $Cu_{64}Zr_{36}$ MG powders during high-temperature oxidation

corresponding to the maximum parabolic rate constants of Powder B and Powder C appears at 873 and 973 K, respectively. The influence of particle size on the oxidation rate of MG powders will be discussed in the next section.

In addition, there is a transition of diffusion mechanism during the long-term oxidation of MG powders. The diffusion process is essentially a thermal activated process, so the oxidation temperature has a great influence on the oxidation rate of MGs. This is mainly reflected in the following two aspects. On the one hand, at the initial stage of oxidation, the oxide layer formed is amorphous, and ions diffuse in the form of accumulated atomic jump due to the existence of excessive free volume in the amorphous matrix [35]. As the temperature rises, the activity of ions increases, and the ion diffusion rate increases,

resulting in the increase of the oxidation rate [26]. On the other hand, with the oxidation temperature increasing towards T_x, the amorphous MG particle interior and the surface oxides will gradually get crystallized, leading to the fast elimination of the free volume. Thus, both the oxide layer and matrix become denser, and it becomes more difficult for ions to diffuse inward, resulting in a decline in the oxidation rate [36]. In the end, the global oxidation rate is determined by these two competitive processes. When the influence of temperature on the thermal activation process is greater than that of the free volume annihilation, the oxide kinetics curve rises, and vice versa. This explains the different variation tendencies of oxidation rates in the first-stage oxidation.

The second-stage oxidation rates of Powder A are close to zero, implying that the oxidation of Powder A mainly occurs at the first stage and gets saturated at the second stage. Meanwhile, the non-zero nature of Powder B and Powder C curves indicates that the oxidation continues at the second stage for these two large-sized powders.

Figure 6 summarizes the final mass gain of powders after oxidation at different temperatures. As implied by the figure, the final mass gain increases monotonically with particle size reduction at all temperatures. That is, the smaller the particle size, the faster the oxidation rate. Meanwhile, for a specific particle size, the final mass gain firstly increases with the temperature rising and reduces after reaching a peak value, which indicates an oxidation mechanism transition induced by high temperature.

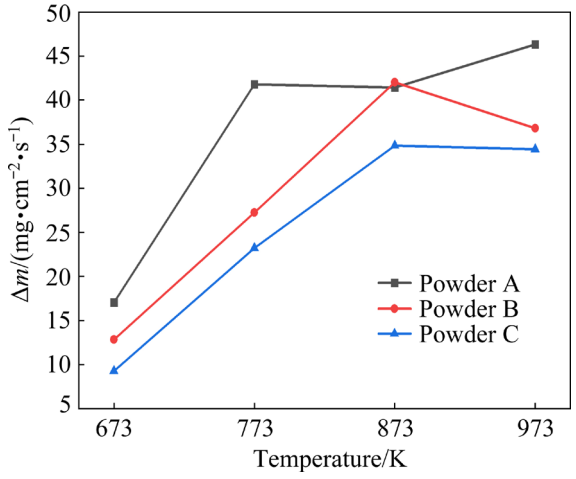

Fig. 6 Final mass gain curves of $Cu_{64}Zr_{36}$ MG powders after high-temperature oxidation

3.3 Oxidation thermodynamics analysis

The influence of particle size on the oxidation rate of MG powders can be explained based on thermodynamics analysis. According to Ref. [37], the oxidation process of MG can be modeled as

$$\Delta_r G_m = \Delta_r G_m^b + \Delta_r G_m^s \tag{2}$$

where $\Delta_r G_m$, $\Delta_r G_m^b$ and $\Delta_r G_m^s$ are the molar total Gibbs free energy change, the molar internal Gibbs free energy change without considering the surface effect, and the molar surface Gibbs free energy change of the system, respectively.

The MG powders are simplified into spheres with the same radius r_M, which refers to the average radius of particles. Hence, $\Delta_r G_m^b$ and $\Delta_r G_m^s$ can be written as

$$\Delta_r G_m^b = \sum \vartheta_M \mu_M^b \tag{3}$$

$$\Delta_r G_m^s = \sum \vartheta_M \mu_M^s = \sum 2\vartheta_M \sigma_M M_M / \rho_M r_M \tag{4}$$

where ϑ_M is the stoichiometric number of the constituent M in the chemical equation of oxidation reaction; μ_M^b and μ_M^s are the internal chemical potential and surface chemical potential of M, respectively; σ_M, M_M, and ρ_M are the surface tension, molar mass, and mass density of M, respectively; r_M is the particle radius. Since only the air/particle interface exists during the powder oxidation, the molar total Gibbs free energy change during MG particle oxidation can be expressed as

$$\Delta_r G_m = \Delta_r G_m^b + 2\vartheta_M \sigma_M M_M / \rho_M r_M \tag{5}$$

And the equilibrium constant K for the oxidation process can be derived as

$$\ln(K/K^b) = -\frac{1}{RT}\Delta_r G_m^s = -2\vartheta_M \sigma_M M_M / (RT\rho_M r_M) \tag{6}$$

For metallic constituents, $\vartheta_M < 0$, hence, $\Delta_r G_m^s$ decreases with the reduction of r_M. According to previous studies, BMG samples ($r_M \to \infty$) also experience notable oxidation, thereby, $\Delta_r G_m^b < 0$. Thus, with the r_M decreasing, the absolute value of $\Delta_r G_m$ keeps increasing (becomes more negative), indicating that the particle is more prone to oxidation. Accordingly, the equilibrium constant K also is greater with the reduction of r_M, implying that powders with smaller particle sizes experience more thorough oxidation.

3.4 Oxidation products

Based on prior experimental results, Powder B with the medium particle size was selected for further characterization of morphology and microstructure, since it presents the most typical phenomena. To determine the oxidation products, Fig. 7 displays the XRD patterns of Powder B after oxidation. As oxidation begins, the powders is crystallized quickly. Even at 673 K, the powders is fully crystallized after 30 min of insulation. At the beginning of oxidation, ZrO_2 phases are first detected, which indicates that Zr is preferentially oxidized in $Cu_{64}Zr_{36}$ MG powders. It is further found that it has two isomers, t-ZrO_2 and m-ZrO_2, and the content of m-ZrO_2 is higher than that of t-ZrO_2. However, Cu immediately diffuses outward at the beginning of oxidation. With the increase of oxidation temperature and oxidation time, a large number of Cu aggregates can be formed, and metallic Cu begins to appear, which is then oxidized into Cu_2O and CuO. It can be seen from Fig. 7 that with the same oxidation time, the higher the oxidation temperature is, the earlier and more oxidation products appear, namely, the faster the oxidation is. This is very reasonable for a thermal activated process.

The surface morphologies of Powder B after 120 min of oxidation are displayed in Fig. 8. It is demonstrated that severe surface precipitation takes place on all observed samples, and the particle surfaces are covered by precipitates with various morphologies. At 673 K, the particle surface is covered by needle-like whiskers. At 773 K, the particle surface is covered by nodule-like structures with some thick needle-like whiskers embedding. As oxidation temperature increases to 873 K, whiskers disappear, and the dimension of nodule-like structures becomes larger. Cracks are also found on the nodule-like structures. While at 973 K, the nodule-like structure seems to "fuse," and the gaps between nodules are filled. In some regions, the nodule-like structure even disappears, and the particle surface becomes smooth. Therefore, it is implied that the surface diffusion or lateral diffusion of ions on the particle surface is enhanced with temperature rising, resulting in the homogenization of oxide growth, i.e., the smoothing of surface oxide morphologies.

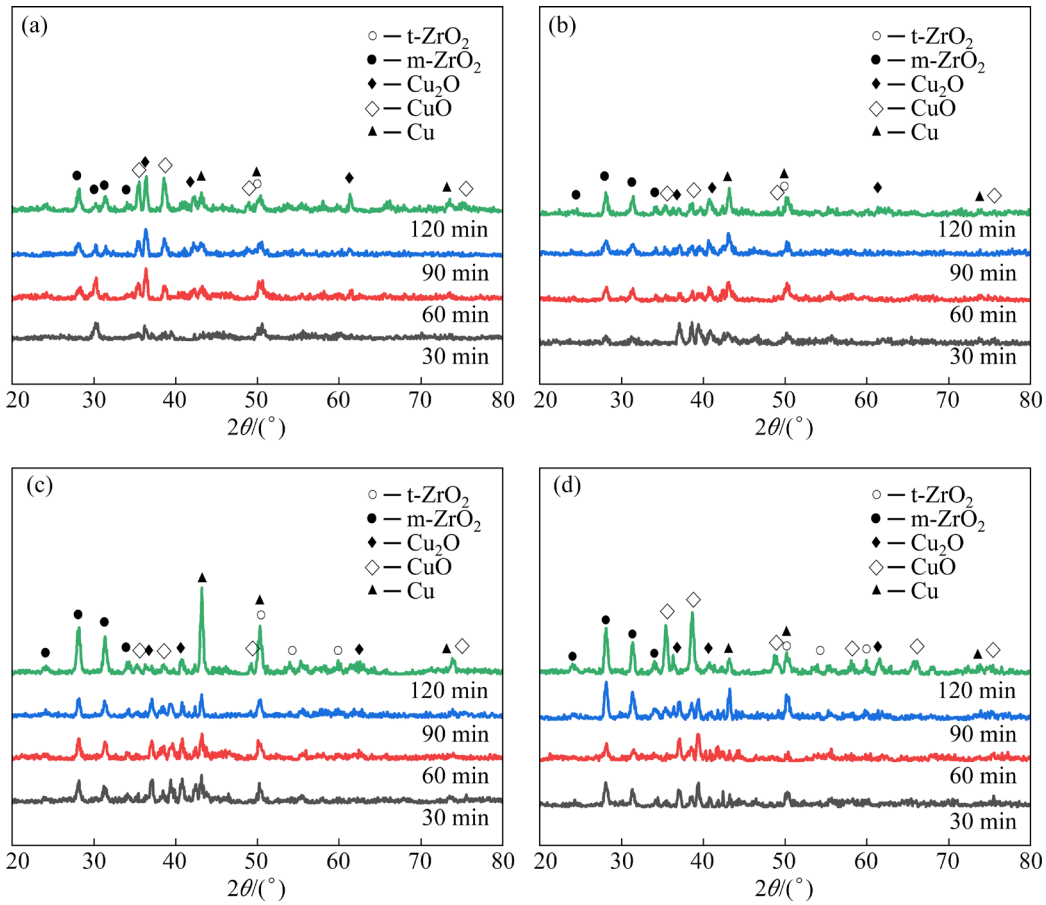

Fig. 7 XRD patterns of Powder B oxidized at 673 K (a), 773 K (b), 873 K (c), and 973 K (d) for different durations

To undercover the detailed structure of surface oxides and reveal their growth mechanisms, TEM analyses were conducted. Special attention was paid to the formation of oxide whiskers at 673 K and oxide cracking at 873 K, the FIB sampling positions of which are labeled in Fig. 8 accordingly.

Figure 9 shows the TEM image and corresponding EDS mappings of the surface layer of Power B oxidized at 673 K for 120 min, the surface morphology of which is displayed in Fig. 8(a). The particle surface is covered by a Cu-enriched layer with a thickness of about 400 nm

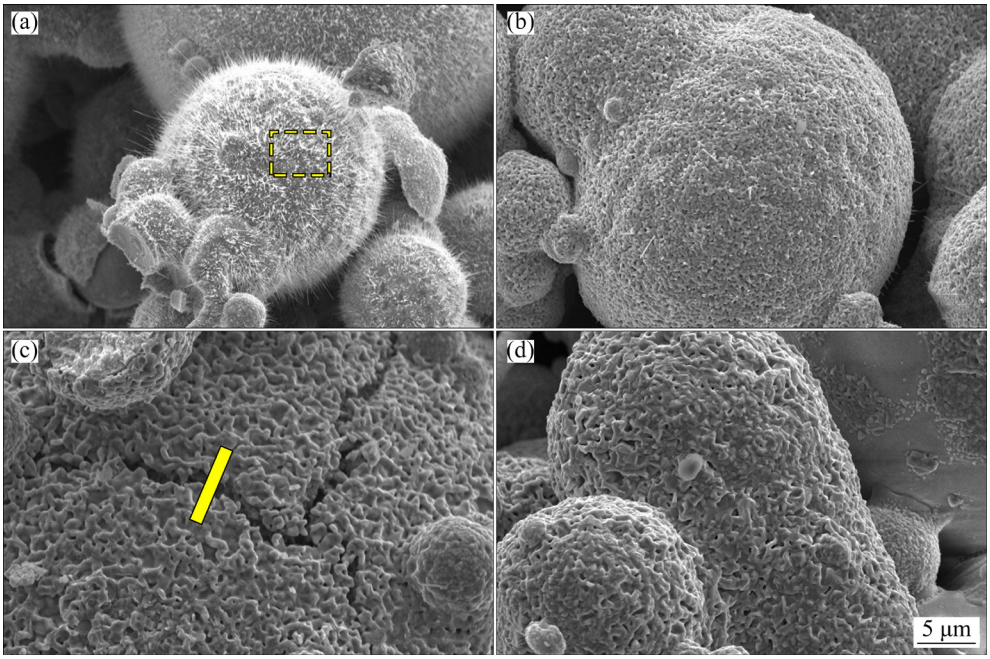

Fig. 8 Surface morphologies of Powder B oxidized for 120 min at 673 K (a), 773 K (b), 873 K (c), and 973 K (d) (The yellow line in (c) indicates the sample position of FIB milling)

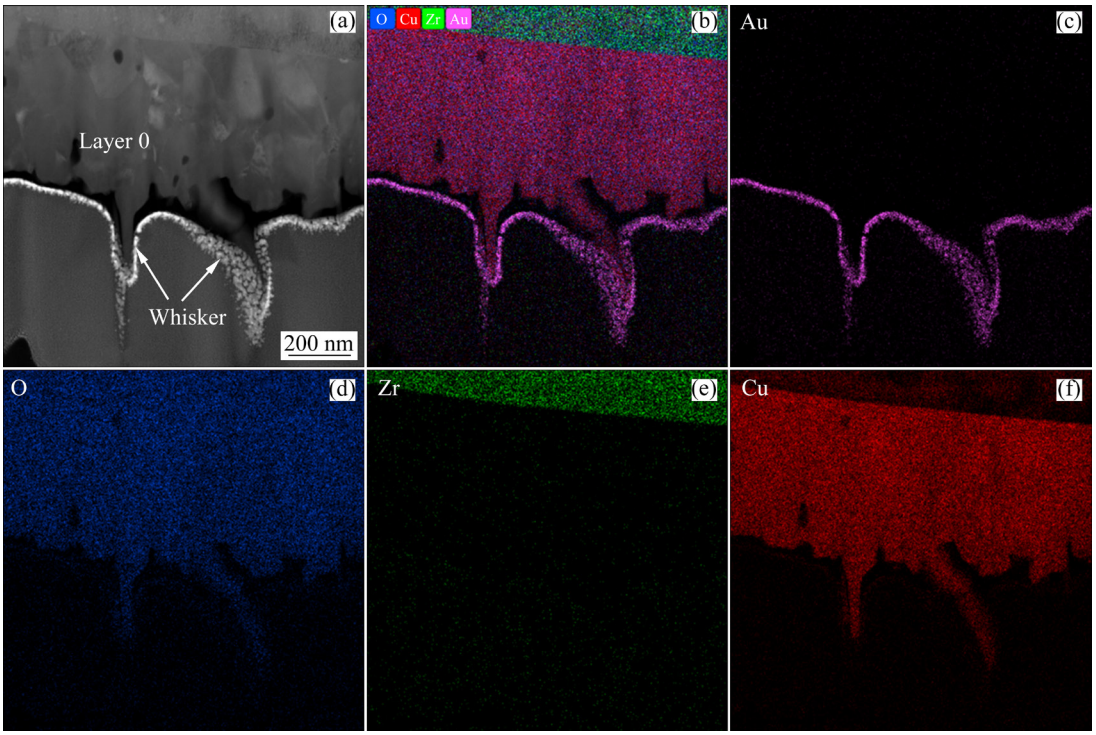

Fig. 9 HAADF-STEM image of surface layer of Powder B oxidized at 673 K for 120 min (a), and EDS mapping of all elements (b), Au (c), O (d), Zr (e), and Cu (f)

(labeled as Layer 0), while Zr is depleted in the surface layer. The Cu-enriched layer consists of equiaxed oxide grains with sizes around 100 nm and needle-like whiskers with diameters about 40 nm. A distinct and straight interface can be found between the Cu-enriched region and the Zr-enriched region, which is suggested to be the original particle surface. According to our previous work, the Cu-enriched layer is a result of the outward diffusion of Cu and the subsequent oxidation of Cu [28] . Since the oxygen affinity of Zr is stronger than that of Cu, Zr and O will preferentially react and form ZrO_2 in-situ [38,39]. Meanwhile, due to the smaller size of Cu and significant compressive stress induced by the formation of ZrO_2 [40], Cu continuously diffuses outward during the oxidation of Zr−Cu-based MGs [26,41].

Figure 10(a) shows the cross-section TEM image of a whisker growing on the surface of the Powder B after oxidation at 673 K for 120 min. According to the HR-TEM image (Fig. 10(b)) and SAED pattern (Fig. 10(d)), it is verified to be a CuO monocrystal. Previous studies have reported that whisker oxides will appear during the oxidation of Cu, Fe, Mo, and Ta under the specific conditions [42]. Whisker oxide usually grows very fast, but it is brittle and easy to break. Due to the deposition of Au on the surface prior to FIB milling, the whiskers are well protected in this study. The formation of this CuO whisker is explained as follows. As shown in Fig. 10(c), a grain boundary triple-junction exists at the root of the monocrystal, which implies that the whisker nucleates from the grain boundary between two CuO grains beneath. Compared to the grain lattice, the grain boundary can act as a short-circuit diffusion path and allow the fast outward transport of massive Cu cations [43].

Moreover, the compressive strain in surface layers can provide the driving force for the growth of whiskers, as indicated by research concerning the Sn whisker growth [44]. During the oxidation of Cu−Zr-based MGs, the formation of oxides will introduce remarkable compressive strain inside the surface scale due to volume expansion, which can act as the driving force for the outward diffusion of

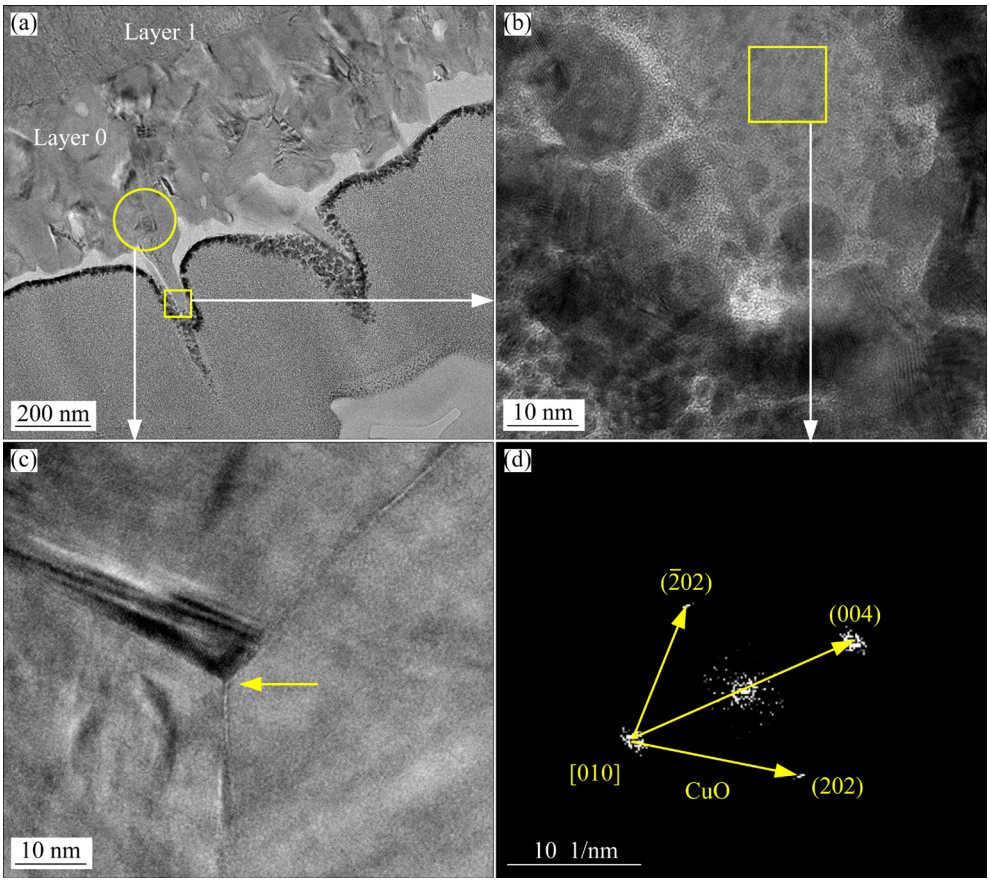

Fig. 10 TEM image of Layer 0 (a), HR-TEM image of oxide whisker (b), HR-TEM image of grain boundary triple-junction beneath oxide whisker (c), and SAED pattern of oxide whisker formed on Powder B oxidized at 673 K for 120 min (d)

Cu cations [45]. Therefore, Cu cations continuously diffuse outward to the whisker root via grain boundaries driven by the compressive strain and feed the rapid growth of CuO monocrystal along specific orientations.

Figure 11 illustrates the structure of the whole oxide scale. Multilayered structures are formed inside the oxide scale, besides the Cu-enriched Layer 0 discussed above. Two layers of Zr-enriched sublayers, labeled as Layer 1 and Layer 2 accordingly, can be distinguished according to the distinct morphologies of oxide grains. As implied by the HAADF-STEM image in Fig. 11(a), these two sublayers consist of columnar oxide dendrites, which can be determined to be ZrO_2 dendrites based on XRD (Fig. 7) and EDS mapping results. This kind of multilayered scale structure can also be found during the oxidation of BMG, as reported in our previous work [28]. As stated above, Layer 0 is formed above the original sample surface due to the outward diffusion of Cu. Meanwhile, Layer 1 and Layer 2 are formed beneath the original sample surface due to the inward diffusion of O and in-situ reaction with Zr. Within Layer 1 and Layer 2, the distributions of Zr and O are relatively homogeneous, while notable Cu-depleted regions can be found near the boundaries between the two layers, as shown in Fig. 11(d). Undoubtedly, this is attributed to the massive outward diffusion of Cu to the surface. Moreover, in Layer 1, fissure-like local Cu-depleted but Zr-enriched regions can also be found, which is attributed to the growth of large ZrO_2 dendrites.

With the increase of insulation temperature, the oxidation behavior of MG powders becomes more complicated. For example, the surface precipitates have greater sizes, and surface cracks appear, as displayed in Fig. 8. Figure 12 shows the cross-section TEM images of the crack depicted in Fig. 8(c). It is displayed that the original surface fractures, and the crack opening is filled up with precipitates. EDS mapping results indicate that the precipitates are Cu oxides, including Cu, Cu_2O, and CuO grains. This is similar to the precipitation behavior in the oxidation process of $Zr_{48}Cu_{36}Al_8Ag_8$ BMG reported by HARATIAN et al [40]. The formation of the crack can be attributed to two aspects. First, the continuous outward diffusion of Cu cations leads to defects, including pores and fissures inside the scale, which provides the nucleus for the origin of cracks [28]. Second, since the Pilling-Bedworth ratio (PBR) of Zr/ZrO_2 is 1.51, the inward diffusion of O and in-situ formation of ZrO_2 will lead to a significant expansion of volume therein [46]. Thus, compressive oxidative stress is triggered and accumulated during the continuous formation of ZrO_2. After the accumulated oxidative stress exceeds the fracture strength of the oxide, cracks are initiated at the nucleus of cracks. During oxidation, the crack provides fast diffusion paths for the outward diffusion of Cu cations and inward diffusion of O anions. The fierce nucleation, growth, and merging of Cu oxide grains on the surface result in the formation of nodule-like morphologies depicted in Fig. 8. Due to the insufficient supply of outward diffusing Cu, there are some pores inside

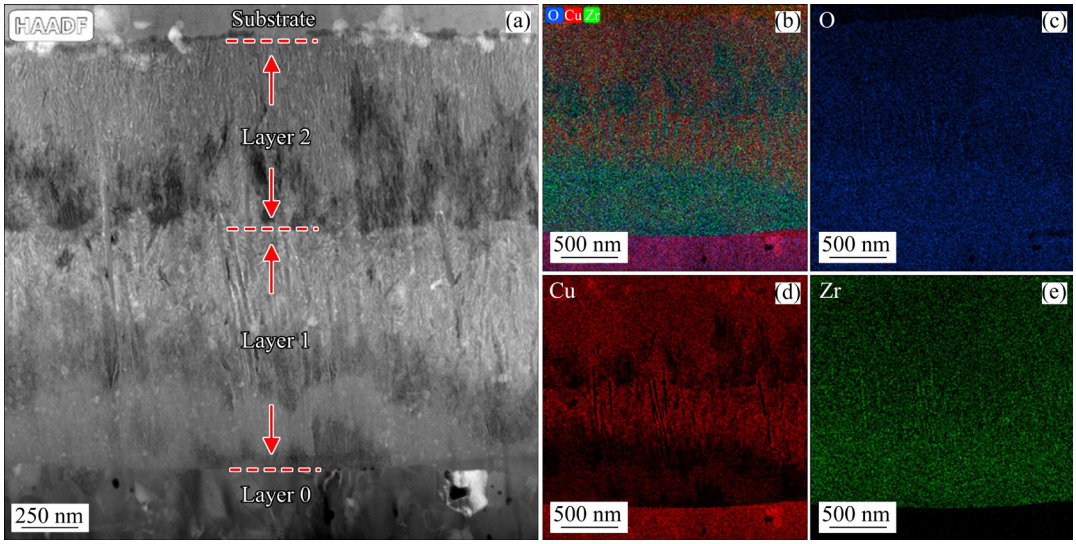

Fig. 11 HAADF-STEM image of oxide scale formed on Powder B oxidized at 673 K for 120 min (a), and EDS mapping images of all elements (b), O (c), Cu (d), and Zr (e)

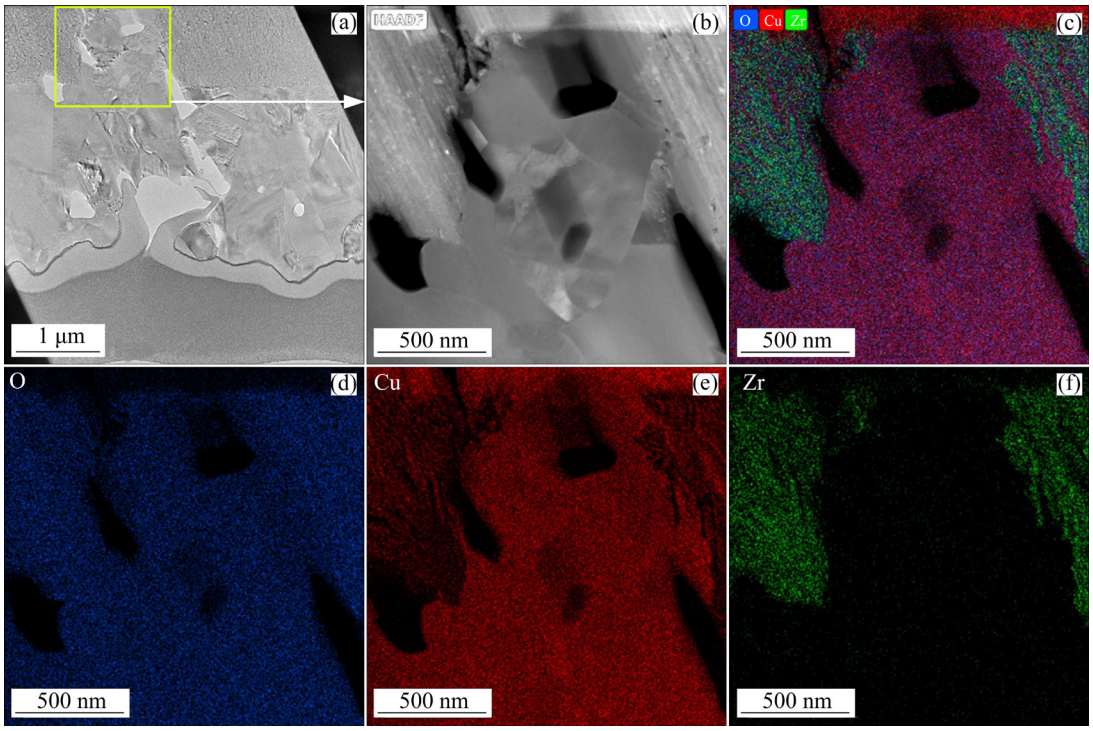

Fig. 12 Cross-section TEM images of crack on surface of Powder B oxidized at 873 K for 120 min (a), HAADF image of crack region (b), and EDS mapping results of all elements (c), O (d), Cu (e), and Zr (f)

the Cu oxides.

It is thereby implied that the notable surface oxidation occurs on the MG powders at high temperatures, either in the glassy state, supercooled liquid state, or crystalline state. The surface morphologies and microstructures are remarkably changed after oxidation, with oxide scales, precipitates, pores, and cracks formed on the surface regions. Moreover, significant elemental redistribution takes place and results in a Cu-enriched layer near the surface. These new phases are certainly unfavorable for the densification and bonding of particles during sintering or 3D printing. Hence, the exposure to the oxidizing atmosphere should be strictly controlled during the preparation, transportation, storage, and utilization of MG powders to avoid surface oxidation.

4 Conclusions

(1) The high-temperature oxidation kinetics of $Cu_{64}Zr_{36}$ MG powders follows the double-stage parabolic rate law. The oxidation process is dominated by the inward diffusion of O anions and the outward diffusion of Cu cations.

(2) The reduction of particle size will enhance the oxidation process, which is attributed to the increase of the absolute value of Gibbs free energy change based on thermodynamics analysis.

(3) Multilayered oxide scales are formed on the surface of MG powders. The notable outward diffusion of Cu cations results in a layer of Cu oxides above the original sample surface, which consists of needle-like oxide whiskers at low temperatures or nodule-like oxides at high temperatures.

Acknowledgments

This work was financially supported by the National Natural Science Foundation of China (No. 51805181), the National Science Fund for Distinguished Young Scholars of China (No. 51725504), and the Fundamental Research Funds for the Central Universities of China (No. 2020kfyXJJS049). The authors are grateful for the technological supports from the Analytical and Testing Center of Huazhong University of Science and Technology, China.

References

[1] SHENG H W, LUO W K, ALAMGIR F M, BAI J M, MA E. Atomic packing and short-to-medium-range order in metallic

glasses [J]. Nature, 2006, 439: 419−425.

[2] WANG W H, DONG C, SHEK C H. Bulk metallic glasses [J]. Materials Science and Engineering R, 2004, 44: 45−89.

[3] QIN C L, ZHANG W, ASAMI K, KIMURA H, WANG X M, INOUE A. A novel Cu-based BMG composite with high corrosion resistance and excellent mechanical properties [J]. Acta Materialia, 2006, 54: 3713−3719.

[4] ZHU Zheng-hou, YIN Lei, HU Qin, SONG Hui. Influence of high-temperature oxidation on soft magnetic properties of $Fe_{78}Si_9B_{13}$ amorphous alloy [J]. Rare Metal Materials and Engineering, 2014, 43: 1037−1040.

[5] LI Ning, XU Xiao-na, ZHENG Zhi-zhen, LIU Lin. Enhanced formability of a Zr-based bulk metallic glass in a supercooled liquid state by vibrational loading [J]. Acta Materialia, 2014, 65: 400−411.

[6] CHU J P, GREENE J E, JANG J S C, HUANG J C, SHEN Y L, LIAW P K, YOKOYAMA Y, INOUE A, NIEH T G. Bendable bulk metallic glass: Effects of a thin, adhesive, strong, and ductile coating [J]. Acta Materialia, 2012, 60: 3226−3238.

[7] SCHUH C A, HUFNAGEL T C, RAMAMURTY U. Overview No.144-Mechanical behavior of amorphous alloys [J]. Acta Materialia, 2007, 55: 4067−4109.

[8] PAN D, GUO H, ZHANG W, INOUE A, CHEN M W. Temperature-induced anomalous brittle-to-ductile transition of bulk metallic glasses [J]. Applied Physics Letters, 2011, 99: 241907.

[9] GONG Pan, WANG Si-bo, LI Fang-wei, WANG Xin-yun. Alloying effect on the room temperature creep characteristics of a Ti−Zr−Be bulk metallic glass [J]. Physica B: Condensed Matter, 2018, 530: 7−14.

[10] NISHIYAMA N, TAKENAKA K, MIURA H, SAIDOH N, ZENG Y Q, INOUE A. The world's biggest glassy alloy ever made [J]. Intermetallics, 2012, 30: 19−24.

[11] SUN Bao-an, WANG Wei-hua. The fracture of bulk metallic glasses [J], Progress in Materials Science, 2015, 74: 211−307.

[12] SURYANARAYANA C, INOUE A. Bulk Metallic Glasses [M]. Boca Raton, London, New York: Taylor & Francis Group, 2011.

[13] DING Da-wei, TAN Jing, CAI An-hui, LIU Yong, WU Hong, AN Qi, LI Peng-wei, ZHANG Yan, YANG Qing. Fe−C micro-alloying effect on properties of $Zr_{53}Al_{11.6}Ni_{11.7}Cu_{23.7}$ bulk metallic glass [J]. Transactions of Nonferrous Metals Society of China, 2021, 31: 2750−2761.

[14] OUYANG Di, XING Wei, LI Ning, LI Yi-cheng, LIU Lin. Structural evolutions in 3D-printed Fe-based metallic glass fabricated by selective laser melting [J]. Additive Manufacturing, 2018, 23: 246−252.

[15] DING Hua-ping, ZHAO Zhan-kui, JIN Jun-song, DENG Lei, GONG Pan, WANG Xin-yun. Densification mechanism of Zr-based bulk metallic glass prepared by two-step spark plasma sintering [J]. Journal of Alloys and Compounds, 2021, 850: 156724.

[16] XIE G Q, LOUZGUINE-LUZGIN D V, INOUE A. Formation and properties of two-phase bulk metallic glasses by spark plasma sintering [J]. Journal of Alloys and Compounds, 2011, 509: S214−S218.

[17] ZHANG Cheng, WANG Wei-hua, LI Yi-cheng, YANG Yan-ge, WU Yue, LIU Lin. 3D printing of Fe-based bulk metallic glasses and composites with large dimensions and enhanced toughness by thermal spraying [J]. Journal of Materials Chemistry A, 2018, 6: 6800−6805.

[18] ZHANG L C, XU J, MA E. Consolidation and properties of ball-milled $Ti_{50}Cu_{18}Ni_{22}Al_4Sn_6$ glassy alloy by equal channel angular extrusion [J]. Materials Science and Engineering A, 2006, 434: 280−288.

[19] LEE S Y, KIM T S, LEE J K, KIM H J, KIM D H, BAE J C. Effect of powder size on the consolidation of gas atomized $Cu_{54}Ni_6Zr_{22}Ti_{18}$ amorphous powders [J]. Intermetallics, 2006, 14: 1000−1004.

[20] ZHENG B L, ASHFORD D, ZHOU Y Z, MATHAUDHU S N, DELPLANQUE J P, LAVERNIA E J. Influence of mechanically milled powder and high pressure on spark plasma sintering of Mg−Cu−Gd metallic glasses [J]. Acta Materialia, 2013, 61: 4414−4428.

[21] XIE G Q, LOUZGUINE-LUZGIN D V, KIMURA H, INOUE A. Nearly full density $Ni_{52.5}Nb_{10}Zr_{15}Ti_{15}Pt_{7.5}$ bulk metallic glass obtained by spark plasma sintering of gas atomized powders [J]. Applied Physics Letters, 2007, 90: 241902.

[22] ZHANG Mao, YAO Di, WANG Xin-yun, DENG Lei. Air oxidation of a $Zr_{55}Cu_{30}Al_{10}Ni_5$ bulk metallic glass at its super cooled liquid state [J]. Corrosion Science, 2014, 82: 410−419.

[23] NA M Y, KIM Y J, KIM W T, KIM D H. Oxidation behavior of Ti−Zr−Ni−Cu metallic glass [J]. Corrosion Science, 2020, 163: 108271.

[24] ZHANG Mao, YAO Di, CAO Zhi-yong, LI Pan, ZHOU Peng, WANG Xin-yun. Influence of oxidation on the performance of $Zr_{55}Cu_{30}Al_{10}Ni_5$ BMG [J]. Intermetallics, 2016, 79: 20−27.

[25] TOFAIL S A M, KOUMOULOS E P, BANDYOPADHYAY A, BOSE S, O'DONOGHUE L, CHARITIDIS C. Additive manufacturing: Scientific and technological challenges, market uptake and opportunities [J]. Materials Today, 2018, 21: 22−37.

[26] WANG B, HUANG D Y, PRUD'HOMME N, CHEN Z, JOMARD F, ZHANG T, JI V. Diffusion mechanism of Zr-based metallic glass during oxidation under dry air [J]. Intermetallics, 2012, 28: 102−107.

[27] LIU L, CHAN K C. Oxidation of $Zr_{55}Cu_{30}Al_{10}Ni_5$ bulk metallic glass in the glassy state and the supercooled liquid state [J]. Applied Physics A, 2005, 80: 1737−1744.

[28] ZHANG Mao, DENG Lei, YAO Di, JIN Jun-song, WANG Xin-yun. Multilayered scale formation during Zr-based metallic glass oxidation in the supercooled liquid region [J]. Corrosion Science, 2016, 111: 556−567.

[29] ZHANG Mao, HUANG Ting, ZHANG Jia-cheng, DENG Lei, GONG Pan, WANG Xin-yun. Influence of oxidation on structure, performance, and application of metallic glasses [ ]. Advanced Materials, 2022, 2110365.

[30] YAN Ming, LI Xiao-peng, YU Peng, SCHAFFER G B, QIAN Ma. Microstructural assessment of the oxidation behavior of Cu-based metallic glass powder [J]. Materials Science Forum, 2010, 654/655/656: 1054−1057.

[31] ZHOU Shang-cheng, ZHANG Peng, XUE Yun-fei, WANG

Fu-chi, WANG Lu, CAO Tang-qing, TAN Zhen, CHENG Bao-yuan, WANG Ben-peng. Microstructure evolution of $Al_{0.6}CoCrFeNi$ high entropy alloy powder prepared by high pressure gas atomization [J]. Transactions of Nonferrous Metals Society of China, 2018, 28: 939−945.

[32] GAO Chao-feng, XIAO Zhi-yu, ZOU Hai-ping, LIU Zhong-qiang, CHEN Jin, LI Shang-kui, ZHANG Da-tong. Characterization of spherical $AlSi_{10}Mg$ powder produced by double-nozzle gas atomization using different parameters [J]. Transactions of Nonferrous Metals Society of China, 2019, 29: 374−384.

[33] WANG Ying, ZHANG Mao, JIN Jun-song, GONG Pan, WANG Xin-yun. Oxidation behavior of CoCrFeMnNi high entropy alloy after plastic deformation [J]. Corrosion Science, 2020, 163: 108285.

[34] PETTIT F S, WAGNER J B Jr. Transition from the linear to the parabolic rate law during the oxidation of iron to wüstite in CO-CO_2 mixtures [J]. Acta Metallurgica, 1964, 12: 35−40.

[35] TANG X P, GEYER U, BUSCH R, JOHNSON W L, WU Yue. Diffusion mechanisms in metallic supercooled liquids and glasses [ ]. Nature, 1999, 402: 160−162.

[36] MEHRER H. Diffusion in solids: Fundamentals, methods, materials, diffusion-controlled processes [M]. Berlin, Germany: Springer, 2007.

[37] ZHANG Mao, DENG Lei, YAO Di, JIN Jun-song, WANG Xin-yun. Effect of surface morphology on the oxidation behavior of bulk metallic glass [J]. Corrosion Science, 2015, 98: 626−633.

[38] WELLER K, WANG Z M, JEURGENS L P H, MITTEMEIJER E J. Oxidation kinetics of amorphous Al_xZr_{1-x} alloys [J]. Acta Materialia, 2016, 103: 311−321.

[39] WELLER K, JEURGENS L P H, WANG Z M, MITTEMEIJER E J. Thermal oxidation of amorphous $Al_{0.44}Zr_{0.56}$ alloys [J]. Acta Materialia, 2015, 87: 187−200.

[40] HARATIAN S, GRUMSEN F B, VILLA M, CHRISTIANSEN T L, SOMERS M A J. Self-repair by stress-induced diffusion of noble elements during oxidation of $Zr_{48}Cu_{36}Al_8Ag_8$ bulk metallic glass [J]. Scripta Materialia, 2019, 164: 126−129.

[41] CAO W H, ZHANG J L, SHEK C H. The oxidation behavior of $Cu_{42}Zr_{42}Al_8Ag_8$ bulk metallic glasses [J]. Journal of Materials Science, 2013, 48: 1141−1146.

[42] WEI Gao, CANTOR B. The oxidation behavior of amorphous alloy $Fe_{40}Ni_{40}P_{14}B_6$ [J]. Acta Metallurgica, 1988, 36: 167−180.

[43] DEVRIES R C, SEARS G W. Growth of aluminum oxide whiskers by vapor deposition [J]. The Journal of Chemical Physics, 1959, 31: 1256−1257.

[44] SOBIECH M, WOHLSCHLÖGEL M, WELZEL U, MITTEMEIJER E J, HÜGEL W, SEEKAMP A, LIU W, ICE G E. Local, submicron, strain gradients as the cause of Sn whisker growth [J]. Applied Physics Letters, 2009, 94: 221901.

[45] HARATIAN S, NIESSEN F, GRUMSEN F B, NANCARROW M J B, PERELOMA E V, VILLA M, CHRISTIANSEN T L, SOMERS M A J. Strain, stress and stress relaxation in oxidized ZrCuAl-based bulk metallic glass [J]. Acta Materialia, 2020, 200: 674−685.

[46] XU C H, GAO W. Pilling-Bedworth ratio for oxidation of alloys [J]. Material Research Innovations, 2000, 3: 231−235.

$Cu_{64}Zr_{36}$ 非晶合金粉末的高温氧化行为

张 茂[1,2]，马云飞[1]，黄 婷[1]，龚 攀[1]，王 颖[3]，蔡洪钧[1]，李巧敏[4]，王新云[1]，邓 磊[1]

1. 华中科技大学 材料科学与工程学院，材料成形与模具技术国家重点实验室，武汉 430074；
2. 燕山大学 亚稳材料制备技术与科学国家重点实验室，秦皇岛 066004；
3. 武汉轻工大学 机械工程学院，武汉 430023；
4. 武汉纺织大学 机械工程与自动化学院，武汉 430073

摘 要：通过气体雾化法制备 $Cu_{64}Zr_{36}$ 非晶合金粉末。采用 XRD、DSC、TGA、SEM 和 TEM 等测试手段研究 $Cu_{64}Zr_{36}$ 非晶合金粉末在内部因素(粉末粒径)和外部因素(氧化温度和氧化时间)影响下的高温氧化行为。分析非晶合金粉末的氧化动力学、氧化物组成、表面形貌和显微组织演变。实验结果表明，$Cu_{64}Zr_{36}$ 非晶合金粉末氧化后表面形成多层氧化物，氧化层主要成分为 t-ZrO_2、m-ZrO_2、Cu_2O 和 CuO。氧化动力学遵循双级抛物线速率定律。氧化过程以 O 离子向内扩散和 Cu 离子向外扩散控制。热力学分析表明，随着粉末粒径的减小，氧化反应的吉布斯自由能变大，导致粒径更小的粉末氧化更为迅速且完全。

关键词：非晶合金粉末；高温氧化；热力学分析；离子扩散；抛物线速率定律

(Edited by Xiang-qun LI)